

LIKELY INTERPOLANTS OF GENERATIVE MODELS

Frederik Möbius Rygaard
 Technical University of Denmark
 fmry@dtu.dk

Shen Zhu
 University of Virginia
 sz9jt@virginia.edu

Yinzhu Jin
 University of Virginia
 yj3cz@virginia.edu

Søren Hauberg
 Technical University of Denmark
 sohau@dtu.dk

Tom Fletcher
 University of Virginia
 ptf8v@virginia.edu

ABSTRACT

Interpolation in generative models allows for controlled generation, model inspection, and more. Unfortunately, most generative models lack a principal notion of interpolants without restrictive assumptions on either the model or data dimension. In this paper, we develop a general interpolation scheme that targets likely transition paths compatible with different metrics and probability distributions. We consider interpolants analogous to a geodesic constrained to a suitable data distribution and derive a novel algorithm for computing these curves, which requires no additional training. Theoretically, we show that our method locally can be considered as a geodesic under a suitable Riemannian metric. We quantitatively show that our interpolation scheme traverses higher density regions than baselines across a range of models and datasets.

Keywords Generative models · Riemannian manifolds · Interpolation · Geometric statistics

1 Introduction

Interpolating samples in generative models is important for generating highly realistic transitions, e.g., for generating “in between” observations and model inspections (Fig. 2). While generative models are able to generate highly realistic samples, interpolation is often done ad hoc, where spherical and linear interpolation often are the go-to standard [Song and Ermon, 2020, Song et al., 2021a, Zheng et al., 2024]. Although these interpolation schemes are simple, they rely on strong assumptions of the model and data dimensionality to approximate the generative data distribution.

Geodesics, which are defined as locally-length minimizing curves on Riemannian manifolds, provide a good starting point for interpolation and has already shown promising results in latent space models, while also providing an operational framework for latent space models [Shao et al., 2018, Arvanitidis et al., 2018, Hauberg, 2019]. Geodesics can be found by minimizing *energy functional* over a suitable set of candidate curves $\gamma : [0, 1] \rightarrow \mathcal{M}$ that connect two points [do Carmo, 1992]

$$\mathcal{E}(\gamma) = \frac{1}{2} \int_0^1 \dot{\gamma}(t)^\top G(\gamma(t)) \dot{\gamma}(t) dt, \quad (1)$$

where G denotes the *metric matrix function* induced by the latent space model. However, geodesics are not always within high-likelihood regions of the data distribution, and for geodesics to have high likelihood, it requires imposing restrictions on the underlying generative model to incorporate data uncertainty into the metric [Hauberg, 2019, Tosi et al., 2014]. Further, this approach assumes access to a latent space equipped with a Riemannian metric. This is

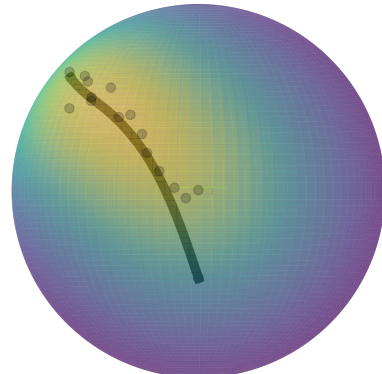


Figure 1: Conceptual illustration of our method: we consider interpolation in generative models as computing curves (black) on a Riemannian manifold constrained to the data distribution (colored).

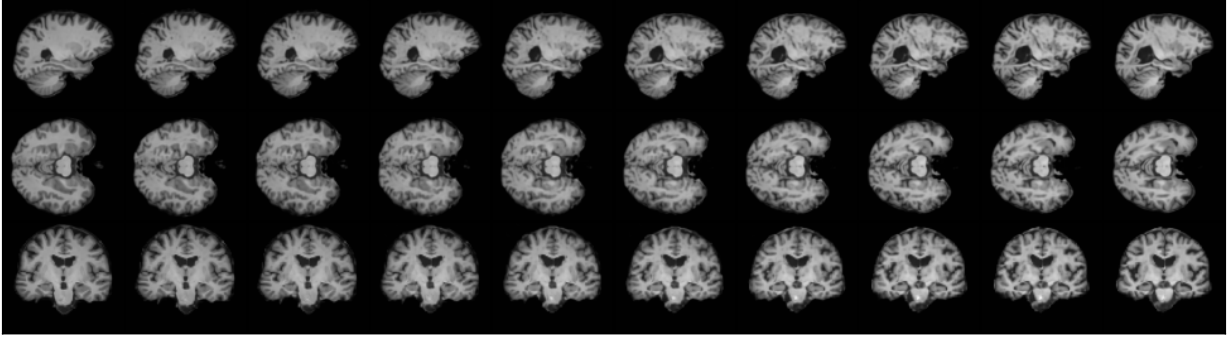


Figure 2: Interpolation using a latent diffusion model similar to [Pinaya et al., 2022] with our proposed method. Each row represents different slices of the brain. The interpolation shows the generative transition between a healthy brain (left) and a brain with Alzheimer disease (right). We show in Section 4 that we obtain a lower Fréchet inception distance (FID) compared to other interpolation schemes.

generally not the case for generative models as, e.g., diffusion models that often apply the ambient Euclidean metric, and in which case geodesic interpolation is simply linear interpolation.

In this paper, we propose a general framework for interpolating in generative models. We consider interpolation analogous to computing a geodesic main support of any given (learned) data distribution providing a trade-off between the smoothness of geodesics and high-density regions (Fig. 1). We introduce a novel algorithm for computing these curves and prove that our algorithm converges to a local minimum and has local quadratic convergence. Further, we show that along the optimal curve, our approach can be seen as a geodesic under a regularized Riemannian metric. Our interpolation approach is applicable to a wide array of generative models. Empirically, we demonstrate it on variational autoencoders, diffusion models, and Riemannian diffusion models, and we show that it obtains curves with a higher likelihood for different models and datasets compared to baselines.

2 Background and related work

Generative models approximates the underlying data distribution, p_{data} , where score-based diffusion models [Song et al., 2021b] accomplish this by transforming the data using forward dynamics:

$$dx_t = \mu(x_t, t)dt + \sigma(t)dW_t, \quad x_0 \sim p_{\text{data}}, \quad (2)$$

such that $\mu : \mathbb{R}^D \times \mathbb{R}_+ \rightarrow \mathbb{R}^D$ and $\sigma : \mathbb{R}_+ \rightarrow \mathbb{R}^D$ are suitable functions for eq. 2 to converge to a known limiting distribution π for a sufficiently large time $T > 0$ [Song et al., 2021b]. Samples from the data distribution can then be generated using the limiting distribution by the time-reversal process $y_t := x_{T-t}$ [Anderson, 1982]:

$$dy_t = (\mu(y_t, t) - \sigma(t)^2 \nabla_y \log p_t(y_t)) dt + \sigma(t)d\bar{W}_t, \quad y_0 \sim \pi, \quad (3)$$

or they can be generated deterministically using the probability flow ODE [Chen et al., 2018]

$$dy_t = \left(\mu(y_t, t) - \frac{1}{2} \sigma(t)^2 \nabla_{y_t} \log p_t(y_t) \right) dt, \quad (4)$$

where $\nabla_y \log p_t(\cdot)$ denotes the *score*, which can be learned using score matching [Hyvärinen, 2005, Vincent, 2011, Song et al., 2020]. The score-based diffusion model can be seen as the continuous version of DDPM [Ho et al., 2020, Song et al., 2021b].

Riemannian manifolds provide a simple principle of interpolation and appear naturally in latent space models like the variational-autoencoder (VAE). Formally, a Riemannian manifold is a differentiable manifold, \mathcal{M} , equipped with a Riemannian metric, in the sense that it defines a smoothly varying inner product, $g : T_x \mathcal{M} \times T_x \mathcal{M} \rightarrow \mathbb{R}$. The inner product is of quadratic form $g(v, w) = v^\top G(x)w$, where $v, w \in T_x \mathcal{M}$ denote elements in the tangent space of \mathcal{M} in $x \in \mathcal{M}$ [do Carmo, 1992]. The tangent space at $x \in \mathcal{M}$ is a vector space that consists of the tangent to all curves at x . The Riemannian metric gives rise to the notion of curves that locally minimize the Riemannian distance:

$$\text{dist}(a, b) := \min_{\gamma} \int_0^1 \sqrt{\dot{\gamma}(t)^\top G(\gamma(t))\dot{\gamma}(t)} dt,$$

with $\gamma(0) = a \in \mathcal{M}$ and $\gamma(1) = b \in \mathcal{M}$. Curves that locally minimize the Riemannian distance are called *geodesics* and can be computed by minimizing the energy functional in eq. 1 [Gallot et al., 2004]. In general, we will assume

that the manifolds studied in this paper are *geodesically complete* in the sense that between any two points, $a, b \in \mathcal{M}$, there exists at least one length-minimizing geodesic connecting the boundary points. Simple examples of a Riemannian manifold are the sphere used in climate data [Karpatne et al., 2019, Mathieu and Nickel, 2020] and the n -dimensional torus used in protein modeling [Lovell et al., 2003, Murray et al., 2003]. More abstract examples of Riemannian manifolds are learned manifolds using latent space models as the VAE, where the decoder under sufficient regularity learns a smooth d -dimensional immersion [Shao et al., 2018, Arvanitidis et al., 2018]. In this case, the Riemannian metric is the pull-back metric from the ambient Euclidean space.

$$G(z) = J_f^\top(z) J_f(z), \quad (5)$$

where J_f denotes the Jacobian of the decoder [Shao et al., 2018, Arvanitidis et al., 2018].

Interpolation in generative models is typically based on strong assumptions about the data dimension and the generative model. Shao et al. [2018], Arvanitidis et al. [2018], Wang and Ponce [2021] propose to use the learned metric for the VAE [Kingma and Welling, 2014] and generative-adversarial network [Goodfellow et al., 2014] (GAN) to compute geodesics for interpolation and extract model information. Although these approaches provide insight into latent space models, they assume a latent space equipped with a Riemannian metric, and it has been observed that for the geodesic to have high likelihood with respect to the data distribution, it requires incorporating data uncertainty directly into the generative model [Hauberg, 2019, Tosi et al., 2014]. Diffusion models do not immediately learn a latent representation of the data, and in this case, the interpolation is computed in the noise distribution that arises as the limit of the forward dynamics [Song et al., 2021b, Song and Ermon, 2020, Du and Mordatch, 2019]. The interpolation scheme is usually linear or spherical interpolation, where spherical interpolation is proposed because in high-dimension an isotropic Gaussian distribution converges to a uniform distribution on a sphere of appropriate radius, assuming that the limiting distribution is isotropic Gaussian. Zheng et al. [2024] extends spherical interpolation to incorporate image editing using pairs of images. Although these methods work well in high-dimensional spaces for Euclidean diffusion models, they are very restrictive on assumptions of dimensionality and the limiting distribution and are, for instance, not applicable to Riemannian diffusion models [Bortoli et al., 2022, Huang et al., 2022, Jo and Hwang, 2024]. Other works train a diffusion model to generate interpolations [Wang and Golland, 2023]. Although this approach shows promising results, it requires additional training and does not relate to any underlying generative model.

3 Probabilistic geodesics

We will formulate our interpolation scheme analogous to computing geodesics restricted to high-density regions of an underlying probability density. We will derive an algorithm to compute these curves as well as show that the curve will locally correspond to geodesics under a Riemannian metric along the optimal curve.

Let \mathcal{M} be a Riemannian manifold. Consider any function $S : \mathcal{M} \rightarrow \mathbb{R}$ that is bounded from below. In the following, we will mostly consider S as the negative log-likelihood along a discretized curve $z_{0:N} := \{z_i\}_{i=0}^N$, that is,

$$S(z) = -\log p(z), \quad (6)$$

where p denotes the generative probability density function. Let $a, b \in \mathcal{M}$ denote two points on \mathcal{M} in local coordinates. To motivate our approach, we estimate the geodesic that connects two points, $a, b \in \mathcal{M}$, with the additional requirement that the geodesic is restricted to regions with high likelihood, i.e., $S(\cdot) < \bar{S}$ for a suitable constant $\bar{S} \in \mathbb{R}$. We therefore consider a discretized version of eq. 1 similar to [Shao et al., 2018, Arvanitidis et al., 2018], but with an additional constraint.

$$\begin{aligned} \min_{z_i} \quad & \sum_{i=0}^{N-1} (z_{i+1} - z_i)^\top G(z_i) (z_{i+1} - z_i) \\ \text{s.t.} \quad & \sum_{i=0}^{N-1} S(z_i) \leq \bar{S}, \quad z_0 = a, z_T = b, \end{aligned} \quad (7)$$

where we use forward differences to discretize the tangent vectors such that $\dot{\gamma}(t_i) \approx N(x_{i+1} - x_i)$. For computational reasons, we instead consider the following minimization problem of the regularized energy functional, which corresponds to a Lagrange relaxation of the constraint in eq. 7.

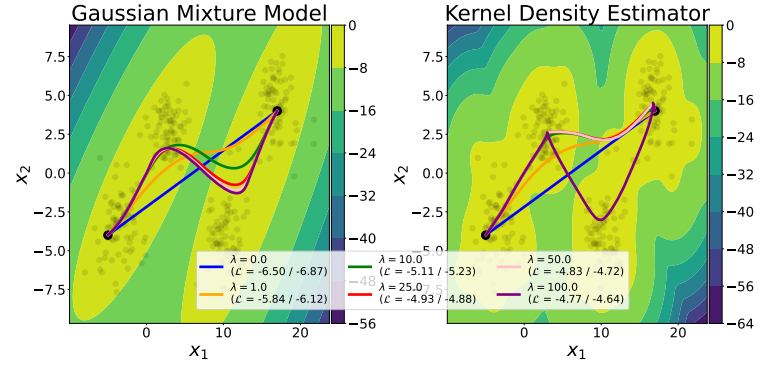
$$\begin{aligned} \min_{z_i} E(z_{0:N}) := \min_{z_i} \quad & \sum_{i=0}^{N-1} \left((z_{i+1} - z_i)^\top G(z_i) (z_{i+1} - z_i) + \lambda S(z_i) \right) \\ \text{s.t.} \quad & z_0 = a, z_N = b, \end{aligned} \quad (8)$$

where $\lambda > 0$ is a dual variable and we have removed any constants from the objective function. If $G(\cdot)$ and $S(\cdot)$ are convex, then there exists a λ such that the solution to the minimization problem in eq. 8 is a solution to the minimization problem in eq. 7. If this is not the case, there could be duality gaps between the minimization problems in eq. 8 and eq. 7, i.e., the solution to eq. 8 is not necessarily a feasible solution to eq. 7.

The minimization problem in eq. 8 provides a trade-off between computing length-minimizing curves and penalizing them by $S(\cdot)$. Thus, a high value of λ will force the constrained geodesic to be in areas where $S(\cdot)$ is small, but will deviate from the geodesic potentially having more non-smooth transitions. We will from now use the minimization problem in eq. 8 to compute interpolated curves. We illustrate the trade-off in Fig. 3 for the density estimated in the Gaussian mixture model (GMM) and the kernel density estimator (KDE) with a Euclidean background metric on synthetic data. We see that higher values of λ force the constrained geodesic into regions with high density, whereas lower values of λ deviate much less from the straight line.

Method We could apply standard optimization algorithms to minimize eq. 8 directly using, e.g., *ADAM* [Kingma and Ba, 2014]. However, computing geodesics without constraints can be computationally difficult and often scales poorly in high dimensions or exhibits slow convergence. Rygaard and Hauberg [2025] circumvent this through an iterative scheme to estimate geodesics with fast convergence using optimal control known as *GEORCE*-algorithm. However, their method does not take into account the regularization of the geodesic. We generalize *GEORCE* to compute geodesics under regularization and prove that our extended method converges to a local minimum (global convergence) with a local quadratic convergence similar to Rygaard and Hauberg [2025].

We formulate the regularized geodesic problem in eq. 8 as a control problem.



$$\begin{aligned}
 \min_{(z_i, u_i)} E(z) := \min_{(z_i, u_i)} & \sum_{i=0}^{N-1} (u_i^\top G(z_i) u_i + \lambda S(z_i)) \\
 \text{s.t. } & z_{i+1} = z_i + u_i, \quad i = 0, \dots, N-1, \\
 & z_0 = a, z_N = b.
 \end{aligned} \tag{9}$$

With this formulation, $z_{0:N}$ denotes the state variables, while $u_{0:(N-1)}$ denotes the control variable such that the control variables correspond to a discretization of the tangent vectors at the grid points of the curve. Since the regularizing function only depends on the state $x_{0:T}$, we can apply a similar approach as Rygaard and Hauberg [2025] to decompose the optimal control problem in eq. 9 into convex subproblems in the control variables. Using this, we show that

Proposition 3.1. *The necessary conditions for a minimum in Eq. 9 is*

$$\begin{aligned}
 2G(z_i)u_i + \mu_i &= 0, \quad i = 0, \dots, N-1, \\
 z_{i+1} &= z_i + u_i, \quad i = 0, \dots, N-1, \\
 \nabla_y [u_i^\top G(y)u_i + \lambda S(y)] \big|_{y=z_i} + \mu_i &= \mu_{i-1}, \quad i = 1, \dots, N-1. \\
 z_0 &= a, z_N = b,
 \end{aligned} \tag{10}$$

where $\mu_i \in \mathbb{R}^d$ for $i = 0, \dots, N-1$.

Proof. See Appendix B.2. □

The necessary conditions in eq. 10 can in general not be solved with respect to $u_{0:(N-1)}$ and $\mu_{0:(N-1)}$. However, we can circumvent this iteratively. In iteration k consider the state and control variables $z_{0:N}^{(k)}$ and $u_{0:(N-1)}^{(k)}$. We fix $G(\cdot)$

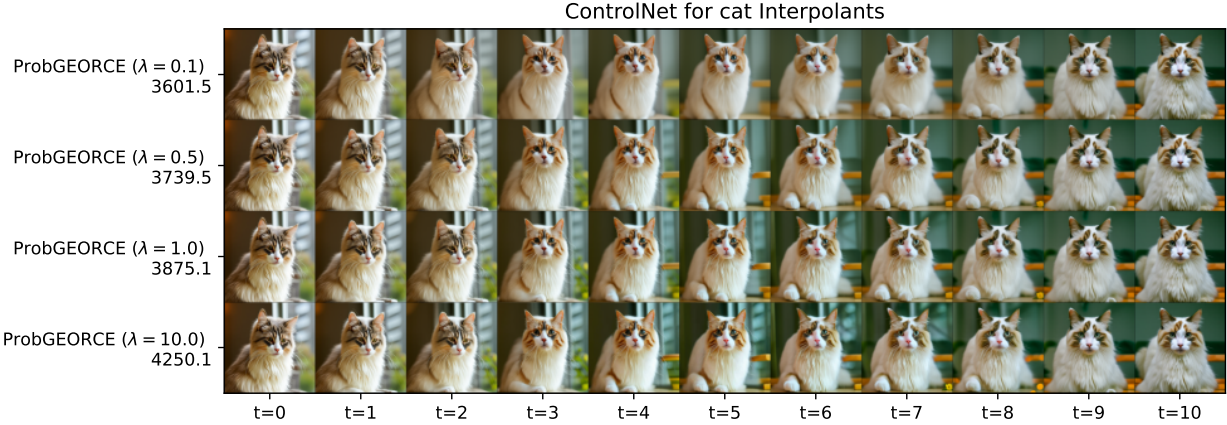


Figure 4: Computed interpolations in noise space for ControlNet [Zhang et al., 2023] for two images of cat of size $768 \times 768 \times 3$ with an Euclidean background metric, where the regularizer function in eq. 6 is the density of the χ^2 -distribution on the norm of the grid points $z_{0:N}$. The left hand side shows the Euclidean energy of the computed curves using eq. 1. We see that larger values of λ reduces smoothness, but increases the image quality as expected.

and the gradient term in iteration k to define the following variables.

$$\begin{aligned} \nu_i &:= \nabla_y (u_i^\top G(y) u_i + \lambda S(y)) \Big|_{y=z_i^{(k)}, u_i=u_i^{(k)}}, \quad i = 1, \dots, N-1, \\ G_i &:= G(z_i^{(k)}), \quad i = 0, \dots, N-1. \end{aligned} \quad (11)$$

With these variables fixed, the system of equations in eq. 10 reduces to

$$\begin{aligned} 2G_i u_i + \mu_i &= 0, \quad i = 0, \dots, N-1, \\ \nu_i + \mu_i &= \mu_{i-1}, \quad i = 1, \dots, N-1, \\ \sum_{i=0}^{N-1} u_i &= b - a, \end{aligned} \quad (12)$$

which naturally leads to the following update scheme.

Proposition 3.2 (Update Scheme). *The update scheme for u_i , μ_i and z_i is*

$$\begin{aligned} \mu_{N-1} &= \left(\sum_{i=0}^{N-1} G_i^{-1} \right)^{-1} \left(2(a-b) - \sum_{i=0}^{N-1} G_i^{-1} \sum_{j>i} \nu_j \right), \\ u_i &= -\frac{1}{2} G_i^{-1} \left(\mu_{N-1} + \sum_{j>i} \nu_j \right), \quad i = 0, \dots, N-1, \\ z_{i+1} &= z_i + u_i, \quad i = 1, \dots, N-1, \\ x_0 &= a. \end{aligned} \quad (13)$$

We denote the algorithm *ProbGEORCE* (Probabilistic GEORCE) and display it in pseudo-code in Algorithm 1 in Appendix A, where we apply line-search in the update scheme using backtracking with parameter $\rho = 0.5$ similar to [Rygaard and Hauberg, 2025]. We note that compared to the original, *GEORCE*-algorithm for unregularized geodesic construction, the only difference between the algorithms is that ν_i depends on $\lambda S(z_i)$. Some generative models, such as diffusion models, apply a Euclidean background metric of high dimension. In this case $G = I$ and storing any matrix would be intractable. However, for a Euclidean metric, the update formulas reduce to

Corollary 3.2.1 (Euclidean Update Scheme). *Assume $G = I$. The update scheme for u_i and z_i is*

$$\begin{aligned} u_i &= \frac{b-a}{N} + \frac{1}{2} \left(\frac{1}{N} \sum_{k=0}^{N-1} \sum_{j>k} \nu_j - \sum_{j>i} \nu_j \right) \quad i = 0, \dots, N-1, \\ x_{i+1} &= x_i + u_i, \quad i = 0, \dots, N-1, \\ x_0 &= a, \end{aligned} \quad (14)$$

where $\nu_i := \lambda \nabla_y S(y) \big|_{y=z_i}$

Thus, for a Euclidean metric, the algorithm has the same complexity as a gradient descent method. We illustrate the scalability of Corollary 3.2.1 to interpolation in noise space for a high-dimensional data using ControlNet [Zhang et al., 2023] in Fig. 4. Here we use the χ^2 -distribution as regularizing function on the norm of z in eq. 6, since the norm of isotropic Gaussian follows a χ^2 -distributions.

Difference in scaling We note that there can be a large difference in scaling between the norm of the score $\sum_{i=0}^{N-1} S(z_i)$ and the energy functional, $\sum_{i=0}^{N-1} u_i^\top G(z_i) u_i$. Let $E^{(0)} = \sum_{i=0}^{N-1} (u_i^{(0)})^\top G(z_i^{(0)}) u_i^{(0)}$ denote the value of the energy functional for the initialization of the curve and, correspondingly, let $S^{(0)} = \sum_{i=0}^{N-1} S(z_i^{(0)})$ denote the sum of the squared norm of the score for the initialization of the curve. We propose to use a normalized version, $\tilde{\lambda}$, in Algorithm 1:

$$\tilde{\lambda} := \lambda \frac{E^{(0)}}{S^{(0)}}.$$

Thus, when $\lambda = 1$, then $E^{(0)}$ and $S^{(0)}$ will have a similar scale, and the weight difference can then be modified by varying λ .

Convergence Under mild assumptions on $S(\cdot)$ we show that *ProbGEORCE* converges to a local minimum (global convergence) and exhibits local quadratic convergence akin to [Rygaard and Hauberg, 2025]. This means that Algorithm 1 converges to a local minimum similar to gradient-based methods and has local convergence similar to the Newton method. We show the details in Appendix B.3.

Local Representation of the Metric Inspired by eq. 8, consider the mapping $F_z(v, w) : v^\top G(z)w + S(z)$. It is clearly seen that this is not linear in the first argument. Thus, S does not define an inner product and, therefore, is not a Riemannian metric. However, we show in the following that along the optimal curve by solving eq. 8 we have a local representation in terms of a Riemannian metric.

Proposition 3.3 (Local Metric). *Let \tilde{S} denote the lower bound of S . Assume that λ is sufficiently large such that $S(\cdot)$ is close to \tilde{S} in eq. 7, and that N is sufficiently large such that $\|z_{i+1}^* - z_i^*\|_2$ is small. Let $\{z_i^*\}_{i=1}^{N-1}$ denote the optimal solution to eq. 8. Then the regularized energy can locally along the optimal curve $\{z_i^*\}_{i=1}^{N-1}$ be estimated as*

$$E(z_{0:N}) \approx \tilde{S} + \sum_{i=0}^{N-1} (z_{i+1}^* - z_i^*)^\top \left(G(z_i^*) + \frac{\lambda}{2} \partial_{zz}^2 S(z_i) \right) (z_{i+1}^* - z_i^*),$$

where $\partial_{zz}^2 S$ denotes the Hessian of S . Thus, if

$$G(z_i^*) + \frac{\lambda}{2} \partial_{zz}^2 S(z_i)$$

is positive definite, we can interpret it as a local representation of a Riemannian metric along the optimal curve.

Proof. See Appendix B.4. □

Connection to other methods Our method regularizes the geodesic interpolation and for $\lambda = 0$ our method will compute the connecting geodesic. In the Euclidean case, geodesic interpolation corresponds to linear interpolation, whereas spherical interpolation corresponds to a geodesic on a sphere. NoiseDiffusion [Zheng et al., 2024] is designed for interpolation in diffusion models with image editing. Let f denote the forward diffusion process that takes data to noise in eq. 2 and f^{-1} denote the reverse process that generates samples of data using noise in eq. 4, then NoiseDiffusion [Zheng et al., 2024] proposes the following interpolation between two images x, y .

$$\begin{aligned} a &= \text{clip}(f(x, t)), \\ b &= \text{clip}(f(y, t)), \\ z_i &= \alpha(i)a + \beta(i)b + (\mu(i) - \alpha(i))x + (\nu(i) - \beta(i))y + \gamma(i)\epsilon, \\ x_i &= f^{-1}(\text{clip}(z_i, t)), \end{aligned} \tag{15}$$

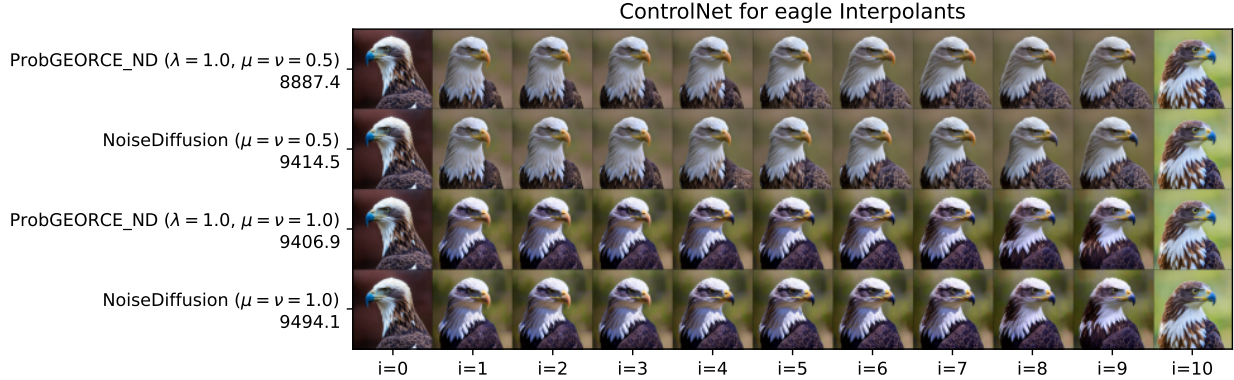


Figure 5: Computed interpolations for ControlNet [Zhang et al., 2023] for eagle images of size $768 \times 768 \times 3$ similar to the experiment by Zheng et al. [2024]. For *ProbGEORCE* we consider a Euclidean background metric, where the regularizer function in eq. 6 is the density of the χ^2 -distribution on the norm of the grid points $z_{0:N}$. The left hand side shows the the Euclidean energy of the computed curves using eq. 1. We see that *ProbGEORCE* obtains similar realism in images with smoother transition compared to *NoiseDiffusion*. Note that *NoiseDiffusion* assumes that the limiting distribution is isotropic Gaussian unlike our method

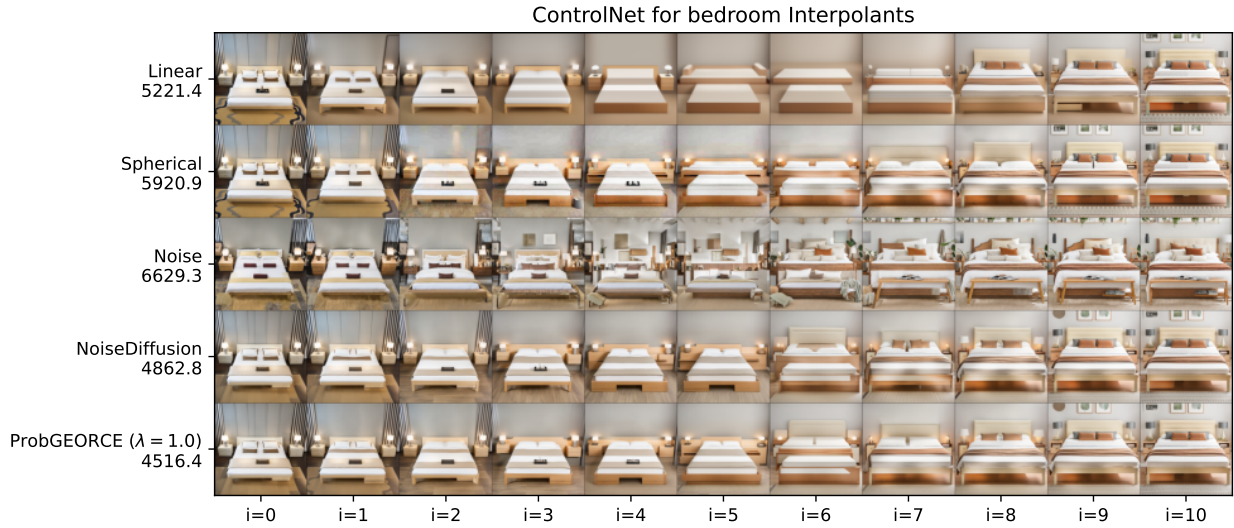


Figure 6: Computed interpolations for ControlNet [Zhang et al., 2023] for bedrooms images of size $768 \times 768 \times 3$. The left hand side shows the the Euclidean energy of the computed curves using eq. 1.

where clip denotes an element-wise operation that restricts a value to be between $[-\text{boundary}, \text{boundary}]$, while $\alpha(i), \beta(i)$ and $\gamma(i)$ are functions depending on i with $\alpha^2(i) + \beta^2(i) + \gamma(i)^2 = 1$ and $\epsilon \sim \mathcal{N}(0, I)$. The functions, $\mu(i)$ and $\nu(i)$, serve as compensation for lost information. Note that

$$z_i = \alpha(i)a + \beta(i)b - \alpha(i)x - \beta(i)y + \mu(i)x + \nu(i)y + \gamma(i)\epsilon.$$

Inspired by eq. 15 we can easily extend our method to compute similar interpolants in noise space by

$$z_i = \text{ProbGEORCE}_1(a, b) - \text{ProbGEORCE}_2(x, y) + \mu(i)x + \nu(i)y + \gamma(i)\epsilon, \quad (16)$$

where $\{\text{ProbGEORCE}\}_{i=1}^2$ denotes the interpolations using Algorithm 1 using any metric or regularization function. Thus, as illustrated in Fig. 5 we can obtain near-identical results to *NoiseDiffusion* with any original images to modify the interpolation curve. Note that *NoiseDiffusion* assumes that the limiting distribution of the diffusion model is isotropic Gaussian, which our modification in eq. 16 does not assume.

4 Experiments

Riemannian diffusion models A natural application of our method is Riemannian diffusion models [Jo and Hwang, 2024], where the forward and backward dynamics in eq. 2 and eq. 3, respectively, are generalized to Riemannian

manifolds using a mixture of diffusion processes. We choose the prior distribution as a wrapped Gaussian and use the log-likelihood of the wrapped Gaussian as regularizer in eq. 6 for the metric, G , of the Riemannian manifold. The interpolation is computed in the noise space, where we generate the samples using a probability flow ODE similar to eq. 4 on Riemannian manifolds [Jo and Hwang, 2024]. In Table 1 we show the log-likelihood for different interpolation curves. We see that our method can compute curves with a higher likelihood, where the optimal value of λ seems to be approximately 0.5.

Interpolation	Earthquake	Flood	Fire	Volcano	\mathbb{H}^4	\mathbb{H}^6
Geodesic	35.25	-108.499	211.914	-241.518	-210.875	-270.270
ProbGEORCE ($\lambda = 0.5$)	36.36	-108.493	202.99	-246.858	-210.872	-270.267
ProbGEORCE ($\lambda = 1.0$)	34.40	-108.681	199.28	-250.006	-210.872	-270.270
ProbGEORCE ($\lambda = 10.0$)	19.64	-115.453	211.80	-209.88	-210.878	-270.272
ProbGEORCE ($\lambda = 100.0$)	26.36	-132.502	200.26	-222.565	-210.873	-270.272

Table 1: Mean log-likelihood numbers for five different interpolation curves for different datasets and manifolds for the mixture of diffusion processes [Jo and Hwang, 2024].

Diffusion models In Euclidean diffusion models, the limiting distribution in eq. 2 is often isotropic Gaussian. The norm of the isotropic Gaussian follows a χ^2 -distribution, which in high dimension converges to a uniform distribution on the sphere, where the radius, d , is the dimension of the data. In this case, spherical interpolation is used for interpolation in the noise space, where the data curve is computed using the ODE in eq. 4. We show that we can obtain results similar to those for spherical interpolation by considering the following regularization function.

$$S(z) = -\lambda_1 \log p(z) + \lambda_2 \|z - \text{Proj}(z)\|_2^2, \quad (17)$$

where p denotes the density of the χ^2 distribution, while Proj denotes the projection onto the sphere of radius d . In practice, we obtain the best results with $\lambda_1 = 1.0$ and $\lambda_2 = 0.1$. We compute the log-likelihood and Fréchet inception distance (FID) for our interpolation curves for different diffusion models. We see in Table 2 that we in general obtain results similar to spherical interpolation, although our method mostly obtains a better FID-score. Zheng et al. [2024] noticed that spherical interpolation sometimes gives non-realistic interpolation curves

Interpolation	OASIS3	CIFAR10 (SGM)	CelebAHQ (SGM)	CIFAR10 (LSGM)	CelebAHQ (LSGM)
Linear	27.83 / 85.94	0.33 / 391.64	-1.61 / 285.32	26.49 / 254.39	1.51 / 149.53
Spherical	28.46 / 68.97	4.30 / 237.64	-1.56 / 142.14	30.00 / 217.10	1.70 / 145.02
ProbGEORCE	28.41 / 66.54	4.12 / 233.84	-0.46 / 138.69	29.99 / 217.52	1.70 / 143.79

Table 2: Mean log-likelihood / FID for interpolation in different diffusion models and datasets. SGM is score-based generative models [Kingma and Ba, 2014], while LSGM is latent score-based generative model [Vahdat et al., 2021]. OASIS3 [LaMontagne et al., 2019] was trained using latent diffusion model [Rombach et al., 2022] used by Pinaya et al. [2022].

and circumvents it by using the image editing in eq. 15. Similarly to the experiments in Zheng et al. [2024], we compute the interpolation between two high-dimensional bedroom images for ControlNet [Zhang et al., 2023], which adds spatial conditioning controls to pre-trained text-to-image diffusion models such as stable diffusion. We use the regularization function in eq. 17, where we set $\lambda_2 = 0$ and clip the interpolation curve between $(-2, 2)$ as proposed by Zheng et al. [2024]. Since we do not have access to a likelihood estimate of the generated samples, we consider the Euclidean energy using eq. 1 with $G = I$ of the interpolation curve in data space. We illustrate the results in Fig. 6 for different interpolation methods, where we see that we obtain results similar to NoiseDiffusion [Zheng et al., 2024] seen in particular in grid $i = 5$, but with smoother transitions. In Appendix C.4 we show additional interpolation curves for the above models compared to different baselines.

Variational autoencoder To further illustrate the flexibility of our method, we compute interpolants that remain in high-density regions for the VAE. The data density is not directly accessible for the VAE, however, the ELBO provides a lower bound of the likelihood of the data distribution. Therefore, we propose to use this as a regularization, i.e.,

$$S(z) = \mathbb{E}_{q_\phi(\tilde{z}|\tilde{x})} [\log p_\theta(\tilde{x}|\tilde{z})] - \text{KL}(q_\phi(\tilde{z}|\tilde{x})||p(\tilde{z})),$$

with a Euclidean metric in the latent space. Since the curve is computed in the latent space, we decode the curve in the data space and

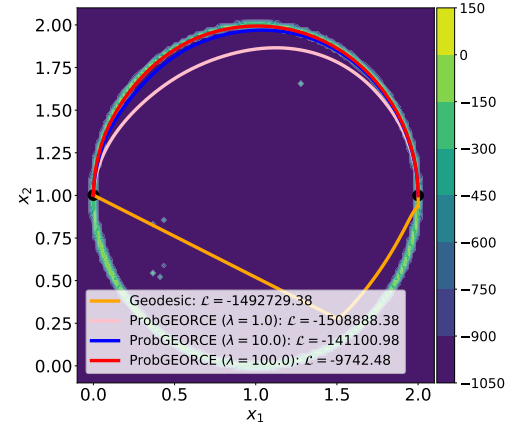


Figure 7: Interpolation curves for a VAE on synthetic data on a circle in \mathbb{R}^3 . The background color denotes the ELBO, where we use 100 Monte Carlo samples to estimate the expectation. We report the numbers in the labels.

consider \tilde{z} as the mean of the encoder and \tilde{x} as the corresponding mean of the decoder to avoid evaluating the expectation using Monte Carlo sampling. We illustrate our method in Fig. 7, where we train a VAE on the unit circle embedded into \mathbb{R}^3 with a two-dimensional latent space and compare to geodesic interpolation using the metric of the decoder in eq. 5. We see that our method accurately follows the data distribution for a sufficiently high λ unlike geodesic interpolation using the metric induced by the decoder as proposed in [Shao et al., 2018, Arvanitidis et al., 2018].

5 Conclusion

In this paper, we have proposed a general approach to computing interpolation in generative models compatible with different metrics and probability distributions. We have derived an algorithm with fast convergence to estimate geodesics constrained to a probability distribution as well as shown that the optimal curve approximately can be seen as a geodesic under a Riemannian metric. Empirically, we have shown our method’s applicability to different generative models and high-dimensional spaces and demonstrated that our interpolation curves are closer to regions with high likelihood.

Limitations Our method shows promising results for computing interpolation for different generative models but requires solving an optimization problem, which is more cumbersome than alternative methods such as linear and spherical interpolation used in diffusion models. Our method assumes a probability distribution and a Riemannian metric. Furthermore, the optimal weight of the regularization, λ and the the choice of regularization function depend on the model and must be fine-tuned.

Acknowledgments

FMR was supported by grants from *Otto Mønsted Fond*, *Knud Højgaard Fond*, *Augustinus Fonden*, *Reinholdt W. Jorck og Hustrus Fond* and *Christian og Ottilia Brorsons Rejselegat* as part of a research stay at the University of Virginia.

References

Brian D.O. Anderson. Reverse-time diffusion equation models. *Stochastic Processes and their Applications*, 12(3):313–326, 1982. ISSN 0304-4149. doi:[https://doi.org/10.1016/0304-4149\(82\)90051-5](https://doi.org/10.1016/0304-4149(82)90051-5). URL <https://www.sciencedirect.com/science/article/pii/0304414982900515>.

Georgios Arvanitidis, Lars Kai Hansen, and Søren Hauberg. Latent space oddity: on the curvature of deep generative models. In *International Conference on Learning Representations*, 2018. URL <https://openreview.net/forum?id=SJzRZ-WCZ>.

Valentin De Bortoli, Emile Mathieu, Michael John Hutchinson, James Thornton, Yee Whye Teh, and Arnaud Doucet. Riemannian score-based generative modelling. In Alice H. Oh, Alekh Agarwal, Danielle Belgrave, and Kyunghyun Cho, editors, *Advances in Neural Information Processing Systems*, 2022. URL <https://openreview.net/forum?id=oDRQGo8I7P>.

Ricky T. Q. Chen, Yulia Rubanova, Jesse Bettencourt, and David K Duvenaud. Neural ordinary differential equations. In S. Bengio, H. Wallach, H. Larochelle, K. Grauman, N. Cesa-Bianchi, and R. Garnett, editors, *Advances in Neural Information Processing Systems*, volume 31. Curran Associates, Inc., 2018. URL https://proceedings.neurips.cc/paper_files/paper/2018/file/69386f6bb1dfed68692a24c8686939b9-Paper.pdf.

M.P. do Carmo. *Riemannian Geometry*. Mathematics (Boston, Mass.). Birkhäuser, 1992. ISBN 9783764334901. URL <https://books.google.dk/books?id=uXJQQgAACAAJ>.

Yilun Du and Igor Mordatch. Implicit generation and modeling with energy based models. In H. Wallach, H. Larochelle, A. Beygelzimer, F. d’Alché-Buc, E. Fox, and R. Garnett, editors, *Advances in Neural Information Processing Systems*, volume 32. Curran Associates, Inc., 2019. URL https://proceedings.neurips.cc/paper_files/paper/2019/file/378a063b8fdb1db941e34f4bde584c7d-Paper.pdf.

S. Gallot, D. Hulin, and J. Lafontaine. *Riemannian Geometry*. Universitext. Springer Berlin Heidelberg, 2004. ISBN 9783540204930. URL https://books.google.dk/books?id=6F4Umpws_gUC.

Ian J. Goodfellow, Jean Pouget-Abadie, Mehdi Mirza, Bing Xu, David Warde-Farley, Sherjil Ozair, Aaron Courville, and Yoshua Bengio. Generative adversarial nets. In Z. Ghahramani, M. Welling, C. Cortes, N. Lawrence, and K.Q. Weinberger, editors, *Advances in Neural Information Processing Systems*, volume 27. Curran Associates, Inc., 2014. URL https://proceedings.neurips.cc/paper_files/paper/2014/file/f033ed80deb0234979a61f95710dbe25-Paper.pdf.

Søren Hauberg. Only bayes should learn a manifold (on the estimation of differential geometric structure from data), 2019. URL <https://arxiv.org/abs/1806.04994>.

Jonathan Ho, Ajay Jain, and Pieter Abbeel. Denoising diffusion probabilistic models. In H. Larochelle, M. Ranzato, R. Hadsell, M.F. Balcan, and H. Lin, editors, *Advances in Neural Information Processing Systems*, volume 33, pages 6840–6851. Curran Associates, Inc., 2020. URL https://proceedings.neurips.cc/paper_files/paper/2020/file/4c5bcfec8584af0d967f1ab10179ca4b-Paper.pdf.

Chin-Wei Huang, Milad Aghajohari, Joey Bose, Prakash Panangaden, and Aaron Courville. Riemannian diffusion models. In Alice H. Oh, Alekh Agarwal, Danielle Belgrave, and Kyunghyun Cho, editors, *Advances in Neural Information Processing Systems*, 2022. URL <https://openreview.net/forum?id=ecevn9kPm4>.

Aapo Hyvärinen. Estimation of non-normalized statistical models by score matching. *Journal of Machine Learning Research*, 6(24):695–709, 2005. URL <http://jmlr.org/papers/v6/hyvainen05a.html>.

Jaehyeong Jo and Sung Ju Hwang. Generative modeling on manifolds through mixture of riemannian diffusion processes. In *Proceedings of the 41st International Conference on Machine Learning*, ICML’24. JMLR.org, 2024.

Anuj Karpatne, Imme Ebert-Uphoff, Sai Ravela, Hassan Ali Babaie, and Vipin Kumar. Machine learning for the geosciences: Challenges and opportunities. *IEEE Transactions on Knowledge and Data Engineering*, 31(8):1544–1554, 2019. doi:10.1109/TKDE.2018.2861006.

Diederik P. Kingma and Jimmy Ba. Adam: A method for stochastic optimization, 2014. URL <http://arxiv.org/abs/1412.6980>. cite arxiv:1412.6980Comment: Published as a conference paper at the 3rd International Conference for Learning Representations, San Diego, 2015.

Diederik P. Kingma and Max Welling. Auto-Encoding Variational Bayes. In *2nd International Conference on Learning Representations, ICLR 2014, Banff, AB, Canada, April 14-16, 2014, Conference Track Proceedings*, 2014.

Pamela J. LaMontagne, Tammie LS. Benzinger, John C. Morris, Sarah Keefe, Russ Hornbeck, Chengjie Xiong, Elizabeth Grant, Jason Hassenstab, Krista Moulder, Andrei G. Vlassenko, Marcus E. Raichle, Carlos Cruchaga, and Daniel Marcus. Oasis-3: Longitudinal neuroimaging, clinical, and cognitive dataset for normal aging and alzheimer disease. *medRxiv*, 2019. doi:10.1101/2019.12.13.19014902. URL <https://www.medrxiv.org/content/early/2019/12/15/2019.12.13.19014902>.

Simon C Lovell, Ian W Davis, W Bryan 3rd Arendall, Paul I W de Bakker, J Michael Word, Michael G Prisant, Jane S Richardson, and David C Richardson. Structure validation by calpha geometry: phi,psi and cbeta deviation. *Proteins*, 50(3):437–450, 2003. doi:doi:10.1002/prot.10286.

Emile Mathieu and Maximilian Nickel. Riemannian continuous normalizing flows. In *Proceedings of the 34th International Conference on Neural Information Processing Systems*, NIPS '20, Red Hook, NY, USA, 2020. Curran Associates Inc. ISBN 9781713829546.

Laura J W Murray, W Bryan 3rd Arendall, David C Richardson, and Jane S Richardson. Rna backbone is rotameric. *Proc Natl Acad Sci U S A.*, 100(24):13904–13909, 2003. doi:doi:10.1073/pnas.1835769100.

Walter H. L. Pinaya, Petru-Daniel Tudosiu, Jessica Dafflon, Pedro F. Da Costa, Virginia Fernandez, Parashkev Nachev, Sébastien Ourselin, and M. Jorge Cardoso. Brain imaging generation with latent diffusion models. In *Deep Generative Models: Second MICCAI Workshop, DGM4MICCAI 2022, Held in Conjunction with MICCAI 2022, Singapore, September 22, 2022, Proceedings*, page 117–126, Berlin, Heidelberg, 2022. Springer-Verlag. ISBN 978-3-031-18575-5. doi:10.1007/978-3-031-18576-2_12. URL https://doi.org/10.1007/978-3-031-18576-2_12.

Robin Rombach, Andreas Blattmann, Dominik Lorenz, Patrick Esser, and Björn Ommer. High-Resolution Image Synthesis with Latent Diffusion Models. In *2022 IEEE/CVF Conference on Computer Vision and Pattern Recognition (CVPR)*, pages 10674–10685, Los Alamitos, CA, USA, June 2022. IEEE Computer Society. doi:10.1109/CVPR52688.2022.01042. URL <https://doi.ieee.org/10.1109/CVPR52688.2022.01042>.

Frederik Möbius Rygaard and Søren Hauberg. Georce: A fast new control algorithm for computing geodesics, 2025. URL <https://arxiv.org/abs/2505.05961>.

Hang Shao, Abhishek Kumar, and P. Thomas Fletcher. The riemannian geometry of deep generative models. In *Proceedings of the IEEE Conference on Computer Vision and Pattern Recognition (CVPR) Workshops*, June 2018.

Jiaming Song, Chenlin Meng, and Stefano Ermon. Denoising diffusion implicit models. In *International Conference on Learning Representations*, 2021a. URL <https://openreview.net/forum?id=St1giarCHLP>.

Yang Song and Stefano Ermon. Improved techniques for training score-based generative models. In H. Larochelle, M. Ranzato, R. Hadsell, M.F. Balcan, and H. Lin, editors, *Advances in Neural Information Processing Systems*, volume 33, pages 12438–12448. Curran Associates, Inc., 2020. URL https://proceedings.neurips.cc/paper_files/paper/2020/file/92c3b916311a5517d9290576e3ea37ad-Paper.pdf.

Yang Song, Sahaj Garg, Jiaxin Shi, and Stefano Ermon. Sliced score matching: A scalable approach to density and score estimation. In Ryan P. Adams and Vibhav Gogate, editors, *Proceedings of The 35th Uncertainty in Artificial Intelligence Conference*, volume 115 of *Proceedings of Machine Learning Research*, pages 574–584. PMLR, 22–25 Jul 2020. URL <https://proceedings.mlr.press/v115/song20a.html>.

Yang Song, Jascha Sohl-Dickstein, Diederik P Kingma, Abhishek Kumar, Stefano Ermon, and Ben Poole. Score-based generative modeling through stochastic differential equations. In *International Conference on Learning Representations*, 2021b. URL <https://openreview.net/forum?id=PxTIG12RRHS>.

Alessandra Tosi, Søren Hauberg, Alfredo Vellido, and Neil D. Lawrence. Metrics for probabilistic geometries. In *Proceedings of the Thirtieth Conference on Uncertainty in Artificial Intelligence*, UAI'14, page 800–808, Arlington, Virginia, USA, 2014. AUAI Press. ISBN 9780974903910.

Arash Vahdat, Karsten Kreis, and Jan Kautz. Score-based generative modeling in latent space. In A. Beygelzimer, Y. Dauphin, P. Liang, and J. Wortman Vaughan, editors, *Advances in Neural Information Processing Systems*, 2021. URL <https://openreview.net/forum?id=P9TYG0j-wtG>.

Pascal Vincent. A connection between score matching and denoising autoencoders. *Neural Computation*, 23(7):1661–1674, 2011. doi:10.1162/NECO_a_00142.

Binxu Wang and Carlos R Ponce. A geometric analysis of deep generative image models and its applications. In *International Conference on Learning Representations*, 2021. URL <https://openreview.net/forum?id=GH7QRzUDdXG>.

Clinton J. Wang and Polina Golland. Interpolating between images with diffusion models, 2023. URL <https://arxiv.org/abs/2307.12560>.

Lvmin Zhang, Anyi Rao, and Maneesh Agrawala. Adding conditional control to text-to-image diffusion models. In *2023 IEEE/CVF International Conference on Computer Vision (ICCV)*, pages 3813–3824, 2023. doi:10.1109/ICCV51070.2023.00355.

PengFei Zheng, Yonggang Zhang, Zhen Fang, Tongliang Liu, Defu Lian, and Bo Han. Noisediffusion: Correcting noise for image interpolation with diffusion models beyond spherical linear interpolation. In *The Twelfth International Conference on Learning Representations*, 2024. URL <https://openreview.net/forum?id=603Q6AFUTu>.

Appendix

A Algorithms

We display *ProbGEORCE* in pseudo-code in Algorithm 1.

Algorithm 1: ProbGEORCE: Probabilistic Geodesics

```

1: Input: tol,  $N$ ,  $\rho$ 
2: Output: Constrained geodesic estimate  $z_{0:N}$ 
3: Set  $z_i^{(0)} \leftarrow a + \frac{b-a}{T}i$ ,  $u_i^{(0)} \leftarrow \frac{b-a}{T}$  for  $i = 0, \dots, N$  and  $k \leftarrow 0$ 
4: while  $\left\| \nabla_y E(y) \Big|_{y=z_i^{(k)}} \right\|_2 > \text{tol}$  with  $E(y)$  defined in eq. 8 do
5:    $G_i \leftarrow G\left(z_i^{(k)}\right)$  for  $t = 0, \dots, T-1$ 
6:    $\nu_i \leftarrow \nabla_y \left( u_i^{(k)} G(y) u_i^{(k)} + S(y) \right) \Big|_{y=z_i^{(k)}}$  for  $i = 1, \dots, T-1$ 
7:    $\mu_{N-1} \leftarrow \left( \sum_{i=0}^{N-1} G_i^{-1} \right)^{-1} \left( 2(a-b) - \sum_{i=0}^{N-1} G_i^{-1} \sum_{j>i}^{N-1} \nu_j \right)$ 
8:    $u_i \leftarrow -\frac{1}{2} G_i^{-1} \left( \mu_{N-1} + \sum_{j>i}^{N-1} \nu_j \right)$  for  $i = 0, \dots, N-1$ 
9:    $z_{i+1} \leftarrow z_i + u_i$  for  $i = 0, \dots, N-1$ 
10:   $j \leftarrow 0$ 
11:  while  $E(z_{0:N}) < E(\tilde{z}_{0:N})$  do
12:     $\tilde{z}_{i+1} = \tilde{z}_i + \rho^j u_i + (1 - \rho^j) u_i^{(k)}$ ,  $i = 0, \dots, N-1$ ,  $\tilde{z}_0 = a$ .
13:     $j \leftarrow j + 1$ 
14:  end while
15:  Set  $u_i^{(k+1)} \leftarrow \rho^{j-1} u_i + (1 - \rho^{j-1}) u_i^{(k)}$  for  $i = 0, \dots, N-1$ 
16:  Set  $z_{i+1}^{(k+1)} \leftarrow z_i^{(k+1)} + u_i^{(k+1)}$  for  $i = 0, \dots, N-1$ 
17:   $k \leftarrow k + 1$ 
18: end while
19: return  $z_i$  for  $i = 0, \dots, N-1$ 

```

B Proofs and derivations

B.1 Assumptions

We will assume the same regularity of the modified energy in eq. 8 as in [Rygaard and Hauberg, 2025] with extra conditions on the regularizing function S . We state these below following the same outline as in [Rygaard and Hauberg, 2025].

Assumption B.1. *We assume the following for the regularized energy in eq. 8.*

- A (local) minimum point $y^* = (z^*, u^*)$ to the regularized energy in eq. 8 is defined as strongly unique minimum point if and only if

$$\exists \epsilon > 0 : \exists K > 0 : \forall z \in B_\epsilon(y^*) : E(y) - E(y^*) \geq K \|z - y^*\|,$$

where $B_\epsilon(y^*) = \{z | \|z - y^*\| < \epsilon\}$.

- We assume that the regularized energy in eq. 8 is locally Lipschitz.

- The first order Taylor approximation of the regularized energy in eq. 8 is

$$\Delta E = \langle \nabla E(y_0), \Delta y \rangle + \mathcal{O}(\Delta y) \|\Delta y\|,$$

i.e., we assume that $\mathcal{O}(\Delta y)$ is independent of z_0 , and the term $\mathcal{O}(\Delta y) \|\Delta y\|$ can be re-written as $\tilde{\mathcal{O}}(\|\Delta y\|^2)$ locally (which follows from the Lipschitz condition).

- We assume that the regularizing function is bounded from below.

B.2 Necessary conditions

Proposition B.1. *The necessary conditions for a minimum in Eq. 9 is*

$$\begin{aligned} 2G(z_i)u_i + \mu_i &= 0, \quad i = 0, \dots, N-1, \\ z_{i+1} &= z_i + u_i, \quad i = 0, \dots, N-1, \\ \nabla_y \left[u_i^\top G(y)u_i + \lambda S(y) \right] \Big|_{y=z_i} + \mu_i &= \mu_{i-1}, \quad i = 1, \dots, N-1. \\ z_0 &= a, z_N = b, \end{aligned} \tag{18}$$

where $\mu_i \in \mathbb{R}^d$ for $i = 0, \dots, N-1$.

Proof. We prove the necessary conditions using the same approach as in [Rygaard and Hauberg, 2025] for the regularized energy function by exploiting Pontryagin's maximum principle. Define the Hamiltonian of the control problem in eq. 9 as

$$H_i(z_i, u_i, \mu_i) = u_i^\top G(z_i)u_i + \lambda S(z_i) + \mu_i^\top (z_i + u_i),$$

which by the time discrete version of Pontryagin's maximum principle gives the following optimization problem

$$\begin{aligned} \min_{u_i} \quad & \sum_{i=0}^{N-1} H_i(z_i, u_i, \mu_i) \\ \text{s.t.} \quad & z_{i+1} = z_i + u_i, \quad i = 0, \dots, N-1 \\ & \nabla_{z_i} H_i(z_i, u_i, \mu_i) = \mu_{i-1}, \quad i = 0, \dots, N-1 \\ & z_0 = a, z_T = b. \end{aligned} \tag{19}$$

Since $G(z_i)$ is positive definite, then $H_i(z_i, u_i, \mu_i)$ is convex in u_i , and therefore the stationary point u_i is also a global minimum point for $i = 0, \dots, N-1$. This gives the following equations for the control problem

$$\begin{aligned} 2G(z_i)u_i + \mu_i &= 0, \quad i = 0, \dots, N-1, \\ x_{i+1} &= x_i + u_i, \quad i = 0, \dots, N-1, \\ \nabla_{x_i} \left(u_i^\top G_i u_i + \lambda S(z_i) \right) + \mu_i &= \mu_{i-1}, \quad i = 1, \dots, N-1, \\ z_0 &= a, z_N = b. \end{aligned}$$

□

B.3 Convergence results

In this section, we generalize the proofs for convergence in [Rygaard and Hauberg, 2025] to include the regularization of the energy.

Proposition B.2 (Global Convergence). *ProbGEORCE in algorithm 1 has global convergence.*

Proof. ProbGEORCE fulfills that

$$\begin{aligned} \nabla_{z_i} E(z, u) \left(z_i^{(k)}, u_i^{(k)} \right) &= \mu_{i-1} - \mu_i, \quad i = 1, \dots, N-1, \\ \nabla_{u_i} E(z, u) \left(z_i^{(k)}, u_i^{(k+1)} \right) &= -\mu_i, \quad i = 0, \dots, N-1, \end{aligned} \tag{20}$$

where

$$E(z, u) := \sum_{i=0}^{N-1} \left(u_i^\top G(z_i)u_i + \lambda S(z_i) \right),$$

and $z_i^{(k)}, u_i^{(k)}$ are the state and control variable at iteration k , respectively. and These properties are identical to the properties for the GEORCE-algorithm in [Rygaard and Hauberg, 2025], and therefore the proof for global convergence for the GEORCE algorithm also holds for ProbGEORCE. □

Proposition B.3 (Local Quadratic Convergence). *ProbGEORCE in algorithm 1 has under the same assumptions as in [Rygaard and Hauberg, 2025] local quadratic convergence in the sense of [Rygaard and Hauberg, 2025], i.e. if the regularized energy functional has a strongly unique (local) minimum point y^* and locally $\alpha^* = 1$, i.e. no line-search, then ProbGEORCE has locally quadratic convergence, i.e.*

$$\exists \epsilon > 0 : \exists c > 0 : \forall y^{(k)} \in B_\epsilon(y^*) : \left\| y^{(k+1)} - y^* \right\|_2 \leq c \left\| y^{(k)} - y^* \right\|_2^2$$

Proof. From eq. 20 the first order Taylor approximation for the regularized energy functional is

$$\begin{aligned}\Delta E(x, u) &= \sum_{i=0}^{N-1} \left\langle -2G\left(y_i^{(k)}\right) \Delta u_i; \alpha \Delta u_i \right\rangle \\ &+ \sum_{i=0}^{N-1} \left(\mathcal{O}\left(\sum_{j=0}^{t-1} \alpha \Delta u_j\right) \left\| \sum_{j=0}^{t-1} \alpha \Delta u_j \right\|_2^2 + \mathcal{O}(\alpha \Delta u_i) \|\alpha \Delta u_i\| \right),\end{aligned}$$

From this the local quadratic convergence proof for *ProbGEORCE* is identical to the local convergence proof for *GEORCE* in [Rygaard and Hauberg, 2025]. Thus, *ProbGEORCE* has quadratic convergence locally. \square

B.4 Local representation of the metric

Proposition B.4 (Local Metric). *Let \tilde{S} denote the lower bound of S . Assume that λ is sufficiently large such that $S(\cdot)$ is close to \tilde{S} in eq. 7, and that N is sufficiently large such that $\|z_{i+1}^* - z_i^*\|_2$ is small. Let $\{z_i^*\}_{i=1}^{N-1}$ denote the optimal solution to eq. 8. Then the regularized energy can locally along the optimal curve $\{z_i^*\}_{i=1}^{N-1}$ be estimated as*

$$E(z_{0:N}) \approx \tilde{S} + \sum_{i=0}^{N-1} (z_{i+1}^* - z_i^*)^\top \left(G(z_i^*) + \frac{\lambda}{2} \partial_{zz}^2 S(z_i) \right) (z_{i+1}^* - z_i^*),$$

where $\partial_{zz}^2 S$ denotes the Hessian of S . Thus, if

$$G(z_i^*) + \frac{\lambda}{2} \partial_{zz}^2 S(z_i)$$

is positive definite, we can interpret it as a local representation of a Riemannian metric along the optimal curve.

Proof. Let $\{z_i^*\}_{i=1}^{N-1}$ denote the optimal solution to eq. 8. A Taylor expansion of S around a point z_i^* gives the approximation

$$S(z_{i+1}^*) = S(z_i^*) + \langle \partial_z S(z_i^*), \Delta z \rangle + \frac{1}{2} \Delta z_i^\top \partial_{zz}^2 S(z_i^*) \Delta z + \mathcal{O}(\Delta z) \|\Delta z\|_2^2,$$

where $\Delta z_i = z_{i+1}^* - z_i^*$ and $\partial_z S(z_i^*)$ and $\partial_{zz}^2 S(z_i^*)$ denote the gradient and Hessian of $S(\cdot)$, respectively. By assumption, \bar{S} is close to the lower bound \tilde{S} , which implies that $\partial_z S(z_i^*) \approx \mathbf{0}$. Similarly, we deduce that $S(z_i^*) \approx \tilde{S}$. The regularized energy in eq. 8 can therefore locally be written as

$$\begin{aligned}E(z_{0:N}) &\approx \tilde{S} + \sum_{i=0}^{N-1} \left((z_{i+1}^* - z_i^*)^\top G(z_i^*) (z_{i+1}^* - z_i^*) + (z_{i+1}^* - z_i^*)^\top \left(\frac{\lambda}{2} \partial_{zz}^2 S(z_i^*) \right) (z_{i+1}^* - z_i^*) \right) \\ &= \tilde{S} + \sum_{i=0}^{N-1} (z_{i+1}^* - z_i^*)^\top \left(G(z_i^*) + \frac{\lambda}{2} \partial_{zz}^2 S(z_i^*) \right) (z_{i+1}^* - z_i^*),\end{aligned}$$

which completes the proof. \square

C Experiments

C.1 Experimental details

For Riemannian diffusion models, SGM, LSTM, and LDM each interpolation curve consists of 10 images in total. We compute the interpolation curves for 5 pairs of images, and calculate the average log-likelihood and FID using these curves.

Riemannian diffusion models For the Riemannian diffusion models we consider a wrapped Gaussian as prior with random mean and scale 1.0 for all models.

ControlNet We use the same prompt as used in Zheng et al. [2024].

Score-based generative modeling On average, sampling an interpolation curve takes around 40s for CIFAR10 and 473s for CelebAHQ.

Latent diffusion model On average, sampling an interpolation curve takes around 13min for OASIS3.

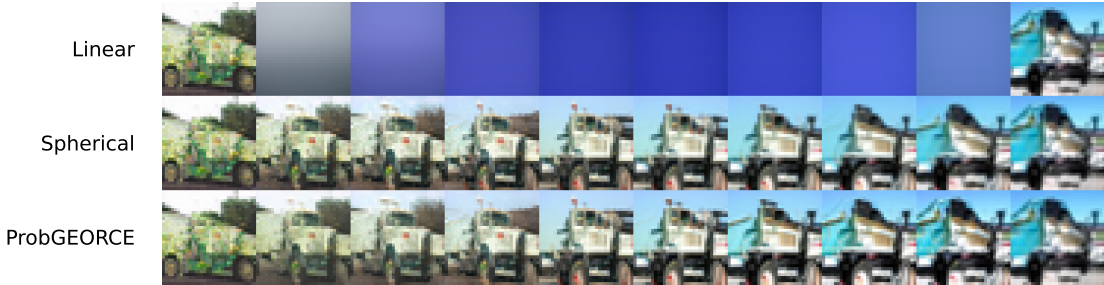


Figure 8: Comparisons of interpolation curves for CIFAR10 with SGM.



Figure 9: Comparisons of interpolation curves for CelebAHQ with SGM.

C.2 Hyperparameters

Score-based generative modeling We choose to use variance exploding SDE (VESDE) for both CIFAR10 and CelebAHQ datasets with SGM. For CIFAR10 interpolation, the minimum σ and maximum σ are set to 0.01 and 50 respectively, with number of scales being 1000. For CelebAHQ interpolation, we use 0.01 and 348 as the minimum and maximum σ . Sampling ϵ is set to $1e - 5$ for both cases. For ProbGEORCE interpolation, we set λ to be 1.0 for both datasets.

Latent score-based generative modeling We choose to use ODE for both CIFAR10 and CelebA datasets with LSGM.

Latent diffusion model We choose to use DDIM for OASIS3 with LDM. Linear β time schedule with 1000 timesteps is adopted with the initial β value being 0.0015 and the last β value being 0.0205.

C.3 Hardware

The interpolation for VAE, GMM and KDE as well as runtime tables have been computed on a: *HP* computer with Intel Core i9-11950H 2.6 GHz 8C, 15.6" FHD, 720P CAM, 32 GB (2×16GB) DDR4 3200 So-Dimm, Nvidia Quadro TI2004GB Descrete Graphics, 1TB PCIe NVMe SSD, backlit Keyboard, 150W PSU, 8cell, W11Home 64 Advanced, 4YR Onsite NBD.

The interpolation for ControlNet and Riemannian diffusion models have been computed on a GPU for at most 24 hours with a maximum memory of 20 GB. The *GPU* consists of 4 nodes on a *Tesla V100*.

The interpolation of CIFAR10 and CelebAHQ with SGM are conducted on a single *Nvidia RTX A6000* GPU with 48G memory.

The interpolation of OASIS3 with LDM are conducted on four *Nvidia RTX A6000* GPUs.

C.4 Additional experiments

ControlNet In Fig. 10, Fig. 10 and Fig. 12 we provide different interpolation curves for ControlNet for different images and interpolation schemes.

Score-Based Generative Models Examples of sampled interpolation curves are shown in 8 and 9.

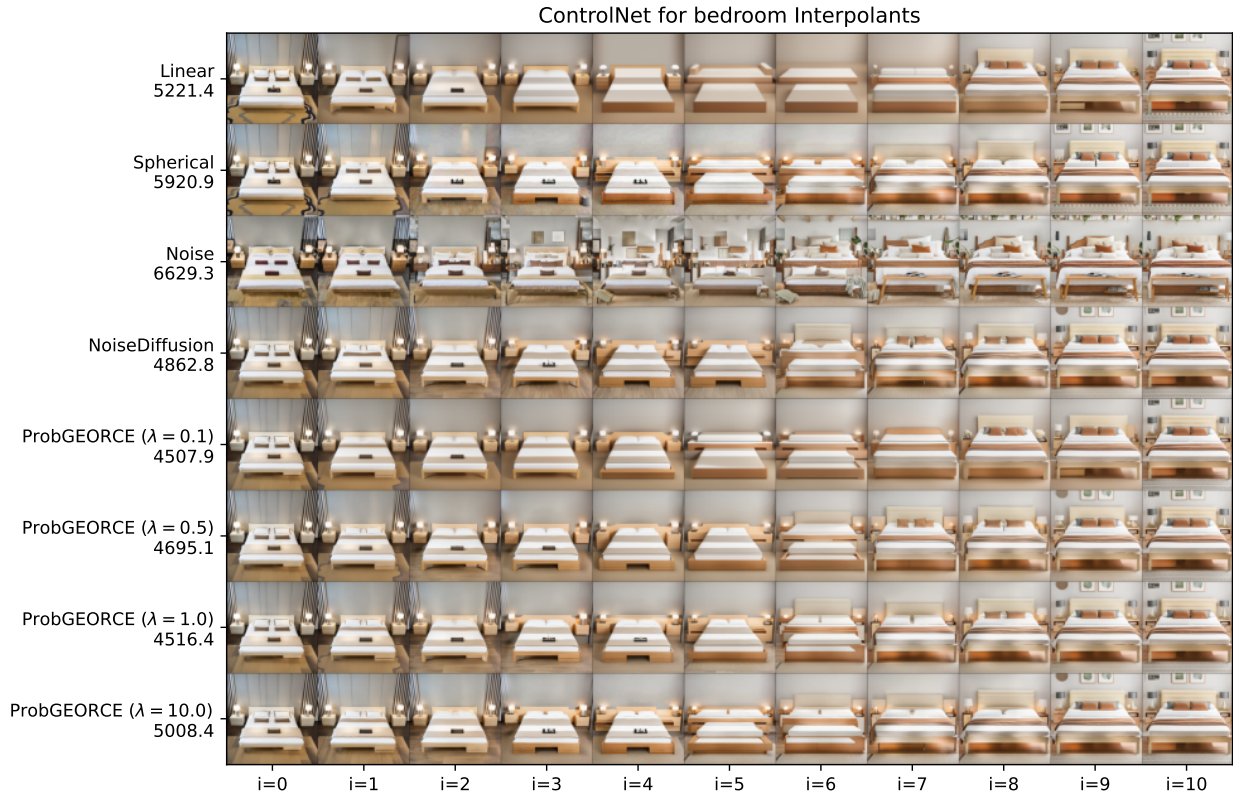


Figure 10: Computed interpolations for ControlNet [Zhang et al., 2023] for bedrooms images of size $768 \times 768 \times 3$. The left hand side shows the the Euclidean energy of the computed curves using eq. 1

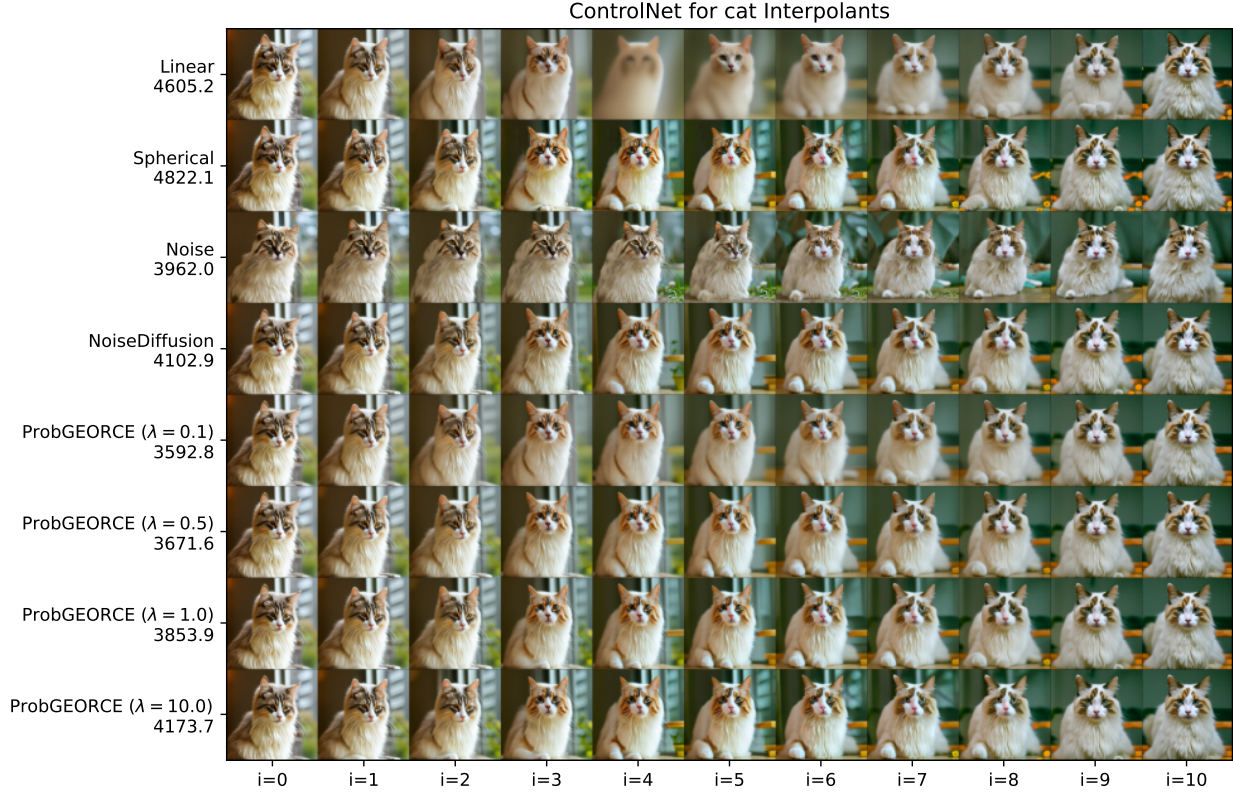


Figure 11: Computed interpolations for ControlNet [Zhang et al., 2023] for cats images of size $768 \times 768 \times 3$. The left hand side shows the the Euclidean energy of the computed curves using eq. 1.

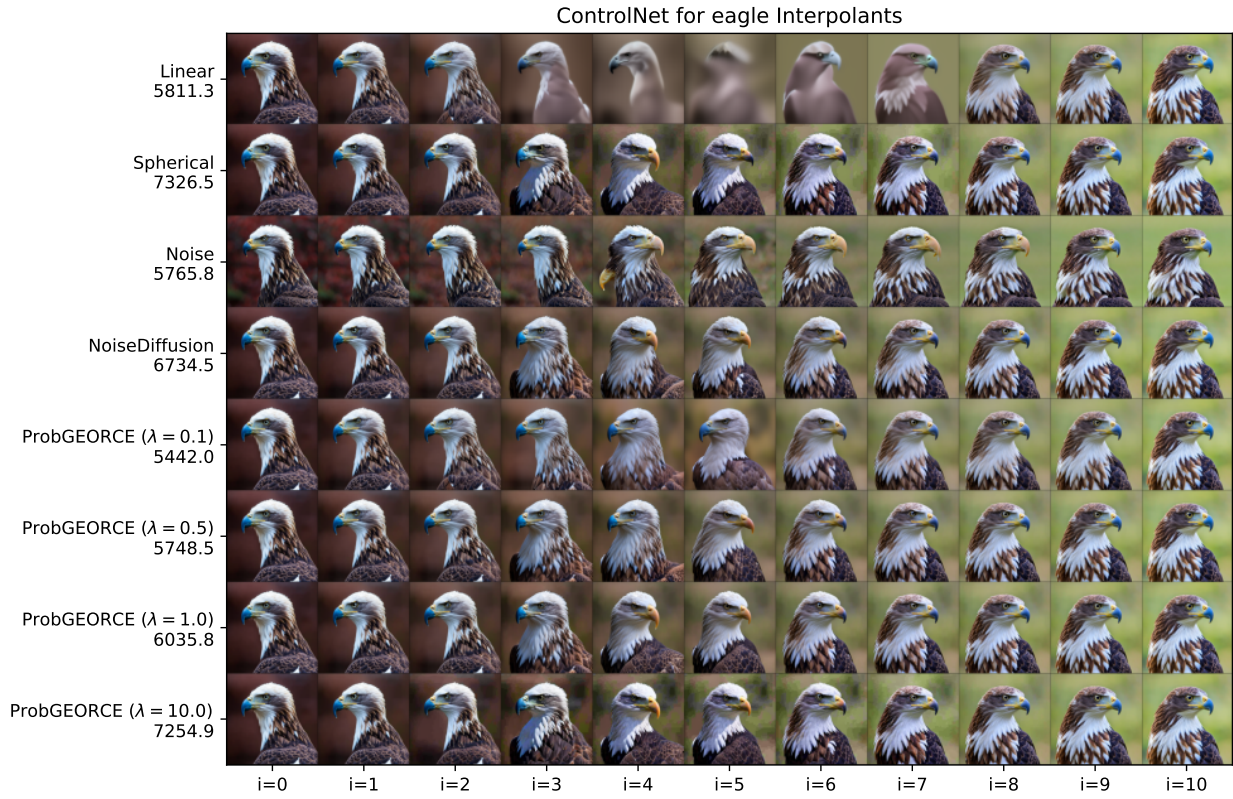


Figure 12: Computed interpolations for ControlNet [Zhang et al., 2023] for eagle images of size $768 \times 768 \times 3$. The left hand side shows the Euclidean energy of the computed curves using eq. 1.